Discrete element simulation of the Jiufengershan rock-and-soil avalanche triggered by the 1999 Chi-Chi earthquake, Taiwan

Kuo Jeng Chang, Alfredo Taboada

Discrete element simulation of the Jiufengershan rock-and-soil avalanche triggered by the 1999 Chi-Chi earthquake, Taiwan

Kuo-Jen Chang[1,2,3] and Alfredo Taboada[1,2]

Received 16 May 2008; revised 21 November 2008; accepted 23 February 2009; published 22 July 2009.

[1] We present Contact Dynamics discrete element simulations of the earthquake-triggered Jiufengershan avalanche, which mobilized a 60 m thick, 1.5 km long sedimentary layer, dipping ~22°SE toward a valley. The dynamic behavior of the avalanche is simulated under different assumptions about rock behavior, water table height, and boundary shear strength. Additionally, seismic shaking is introduced using strong motion records from nearby stations. We assume that seismic shaking generates shearing and frictional heating along the surface of rupture, which, in turn, may induce dynamic weakening and avalanche triggering; a simple ''slip-weakening'' criterion was adopted to simulate shear strength drop along the rupture surface. We investigate the mechanical processes occurring during triggering and propagation of an avalanche mobilizing shallowly dipping layers. Incipient deformation forms a pop-up structure at the toe of the dip slope. As the avalanche propagates, the pop-up deforms into an overturned fold, which overrides the surface of separation along a décollement. Simultaneously, uphill layers slide at high velocity (125 km/h) and are folded and disrupted as they reach the toe of the dip slope. The avalanche foot forms a wedge that is pushed forward as deformed rocks accrete at its rear. We simulated five cross sections across the Jiufengershan avalanche, which differ in the geometry of the surface of separation. Topographic and simulated surface profiles are similar. The friction coefficient at the surface of separation determined from back analysis is abnormally low ($\mu_{SS} = 0.2$), possibly due to lubrication by liquefied soils. The granular deposits of simulated earthquake- and rain-triggered avalanches are similar.

Citation: Chang, K.-J., and A. Taboada (2009), Discrete element simulation of the Jiufengershan rock-and-soil avalanche triggered by the 1999 Chi-Chi earthquake, Taiwan, *J. Geophys. Res.*, *114*, F03003, doi:10.1029/2008JF001075.

1. Introduction

[2] The Chi-Chi Taiwan earthquake (21 September 1999, $M_L = 7.3$, $M_W = 7.6$) caused much damage and triggered more than 10,000 landslides [*National Center for Research on Earthquake Engineering*, 1999; *Liao*, 2000], most of which were located in the hanging wall of the Chelungpu fault [*Wang et al.*, 2003b]. The Jiufengershan avalanche was the second largest landslide triggered by the Chi-Chi earthquake, mobilizing about 42×10^6 m^3 of rock and soil from a dip slope [*Chang et al.*, 2005a]. The avalanche located about 12 km to the north of the epicenter (120.84°E, 23.96°N), destabilized the western limb of the Taanshan syncline along an inferred weak stratigraphic layer. It mobilized a ~60 m thick and 1.5 km long layer of Miocene shales and sandstones, which dipped ~22°SE toward a valley. It involved a ''flatiron'' remnant that was entirely mobilized during the earthquake. The weathered and jointed materials were transported downslope for about 1 km, creating a deep-seated rock-and-soil avalanche [*Chang et al.*, 2005a]. The avalanche was slowed by N-S trending ridges located downstream along the Jiutsaihu creek. The rock-and-soil debris were deposited against several hills, infilling gorges and damming two creeks.

[3] Earthquake-triggered avalanches are among the most dynamic surface processes involved in landscape evolution. The mechanics of such processes is largely unknown and is still a matter of debate [e.g., *Jibson*, 1996]. However, several numerical methods exist to study the initiation and the motion phases of slope failures triggered by earthquakes.

[4] The initiation has been traditionally studied by limit equilibrium methods [e.g., *Ambraseys*, 1960; *Seed*, 1979], and more recently, by discrete element methods [e.g., *Havenith et al.*, 2003]. Limit equilibrium methods are based on calculation of a factor of safety, which measures the susceptibility to slope failure along a critical slip surface [e.g., *Locat et al.*, 2004; *Moon and Blackstock*, 2004]. The stresses induced by an earthquake are represented by a set of external forces applied to the potential sliding mass (pseudostatic approach) [*Del Gaudio et al.*, 2000; *Moon*

[1]UMR 5243, Géosciences Montpellier, Université Montpellier II, INSU, CNRS, Montpellier, France.
[2]ADEPT, International Associated Laboratory, NSC, CNRS, Rennes, France.
[3]Department of Civil Engineering, National Taipei University of Technology, Taipei, Taiwan.

0148-0227/09/2008JF001075

and Blackstock, 2004]. Alternatively, discrete element methods are based on estimation of contact forces and relative displacements between rigid or deformable blocks that compose fractured or jointed hillslopes [e.g., *Itasca*, 2000]. Using the latter, *Havenith et al.* [2003] modeled initiation of a rockslide and a debris flow in jointed hillslopes in Kyrgyzstan. These authors analyzed the deformation mechanisms (e.g., block tilting and slip) leading to formation of a slip surface.

[5] The motion phase has been analyzed using block-on slope analyses, continuum mechanics, and discontinuous mechanical approaches. The block-on slope methods calculate cumulative displacements of a sliding block, induced by seismic shaking [*Newmark*, 1965]. The block moves when the sum of the static and dynamic driving forces exceeds the shear strength along the slip surface. This method has been adapted to calculate the displacement of several landslides [*Wilson and Keefer*, 1983; *Jibson*, 1996; *Chugh and Stark*, 2006; *Ingles et al.*, 2006]. *C. C. Huang et al.* [2001] applied this method to the Jiufengershan avalanche to estimate the kinematic conditions required for large-scale failure. Using a block-on slope model, *Chang et al.* [2005b] analyzed both triggering and motion of the Jiufengershan avalanche by introducing frictional heating and pore pressure increase in the basal shear plane.

[6] Continuum mechanics methods based on large-strain formulations have also been used to estimate deformation and displacement of a soil mass subjected to earthquake shaking [*Chugh and Stark*, 2006]. This approach is potentially efficient, but numerically intensive as shown by recent applications using the computer program FLAC [*Itasca*, 2000]: calculation of a 2 m displacement for a 200 m long shallow landslide required over 240 h on a well equipped personal computer [*Chugh and Stark*, 2006].

[7] Discrete element methods are well suited to study deformation processes involving large strains. As an example, *J. H. Wu et al.* [2005] studied postfailure motion of the lower slope of the Jiufengershan avalanche, using a discrete element analysis based on minimization of potential energy. The unstable rock mass was modeled as 34 blocks interacting by means of normal contact springs and Coulomb-type shear forces. However, the geometry of the simulated debris deposit seems unrealistic since the blocks are large and do not fracture during the avalanche.

[8] A reliable simulation of an avalanche should integrate the triggering and the motion phases within the same model. In spite of advances in modeling techniques, we are not aware of realistic simulations of earthquake-triggered avalanches integrating the complete process.

[9] Hence, we present numerical simulations of initiation and motion of the Jiufengershan rock-and-soil avalanche triggered by the Chi-Chi (1999) Taiwan earthquake [*Chang et al.*, 2005a], which provide new insights into the behavior of these surface instabilities.Our numerical models utilize geological, geotechnical, morphological, and seismological data sets. This work aims to identify mechanical processes and deformation mechanisms involved in earthquake-triggered avalanches that mobilize shallow dipping layers; influences of specific triggering mechanisms (earthquake or rainfall) on avalanche dynamics, are also discussed. Detailed implementation of the simulation technique is given by the companion paper [*Taboada and Estrada*, 2009].

[10] Seismic shaking is introduced in the model through strong motion acceleration records from the Chi-Chi earthquake. The stability of the dip slope is analyzed for three different materials and for different water table heights. Additionally, we perform simulations for five avalanche cross sections, which differ in the geometry of the surface of separation (SS) (e.g., horizontal, updipping, or downdipping). Finally, avalanche initiation is analyzed in terms of particle contact forces.

[11] The landslide area geology and description of the avalanche are presented in section 2. In section 3, a behavior law of the granular layers is calibrated to simulate intact rock, weathered rock, and weakly weathered rock. Field data and hypotheses concerning groundwater flow, pore pressure, dynamic weakening of the slip surface, and strong motion records are also presented in section 3. The results of numerical simulations are detailed in section 4. The main findings are summarized and discussed in section 5.

2. Geological Setting and Landslide Occurrence

[12] The Taiwan orogenic belt results from the rapid convergence between the Luzon volcanic arc, which is part of the Philippine Sea Plate (PSP), and the passive Eurasian continental margin (Figure 1). The PSP is moving at a relative velocity of 8.2 cm/a toward the NW in relation to the Eurasian continental margin [*Yu et al.*, 1997]. The oblique arc-continent collision began during the late Miocene, creating east-dipping thrusts and folds. Active deformation migrated progressively northward and westward, affecting successively the sediments deposited in foreland basins [*Suppe*, 1981; *Covey*, 1984; *Lacombe et al.*, 2001; *Mouthereau et al.*, 2001]. The Chi-Chi Taiwan earthquake (21 September 1999) is associated with the Chelungpu thrust fault, whose current kinematics is consistent with oblique plate convergence [*Shin et al.*, 2000; *Angelier et al.*, 2001; *Kao and Angelier*, 2001].

[13] The Jiufengershan rock-and-soil avalanche is located in the Western Foothill orogenic belt characterized by west vergent imbricate folds and thrusts (inset in Figure 1) [*Suppe and Namson*, 1979; *Suppe*, 1980, 1981; *Hung and Wiltschko*, 1993]. This belt consists of Late Oligocene to Miocene sedimentary rocks [*Y. C. Huang*, 1986; *L. C. Wu*, 1986; *Mao et al.*, 2002]. The stratigraphic formations from

Figure 1. Geological map and cross section of the Jiufengershan avalanche area (indicated by the square in the inset). The topographic profile before the slide is indicated in cross section A-A′ by a dotted line. The profiles A, B, C, D, and E are analyzed in the numerical simulations (Figure 6). SA, sliding area (purple); DA, deposit area (orange); DP, dipping plane; FB, frontal backstop; SS, surface of separation; h_w, water table height above the DP; TL, Tanliaoti Shale; SMb, SMm, SMt, bottom, middle, and top members, respectively, of Shihmen Formation (SM); CHb, CHm, CHt, bottom, middle, and top members, respectively, of Changhukeng Shale; KC, Kueichulin Formation; SF, Shuilikeng fault; TS, Taanshan syncline. Open circles indicate core holes.

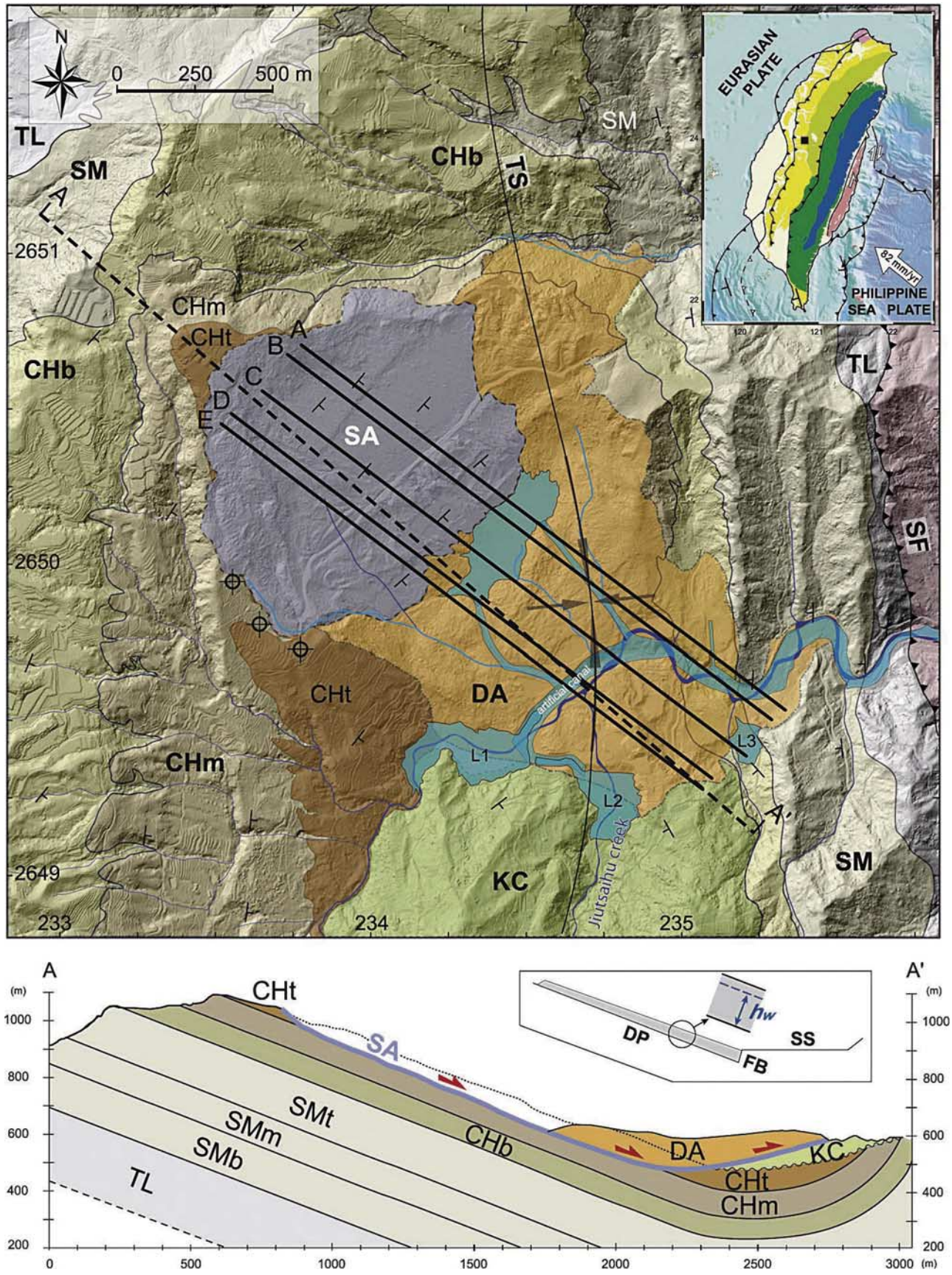
N
0 250 500 m
TL
SM
CHb
TS
SM
A
2651
CHm
CHt
B
C
D
E
A
CHb
SA
TL
SF
2650
CHt
DA
artificial canal
L1
L3
L2
CHm
A'
2649
KC
Jiutsaihu creek
SM
233
234
235
EURASIAN PLATE
PHILIPPINE SEA PLATE
82 mm/yr
120
121
22
23
24
A
A'
(m)
1000
800
600
400
200
CHt
SA
SMt
SMm
SMb
TL
CHb
DA
KC
CHt
CHm
hw
DP
SS
FB
0
500
1000
1500
2000
2500
3000
(m)

Figure 1

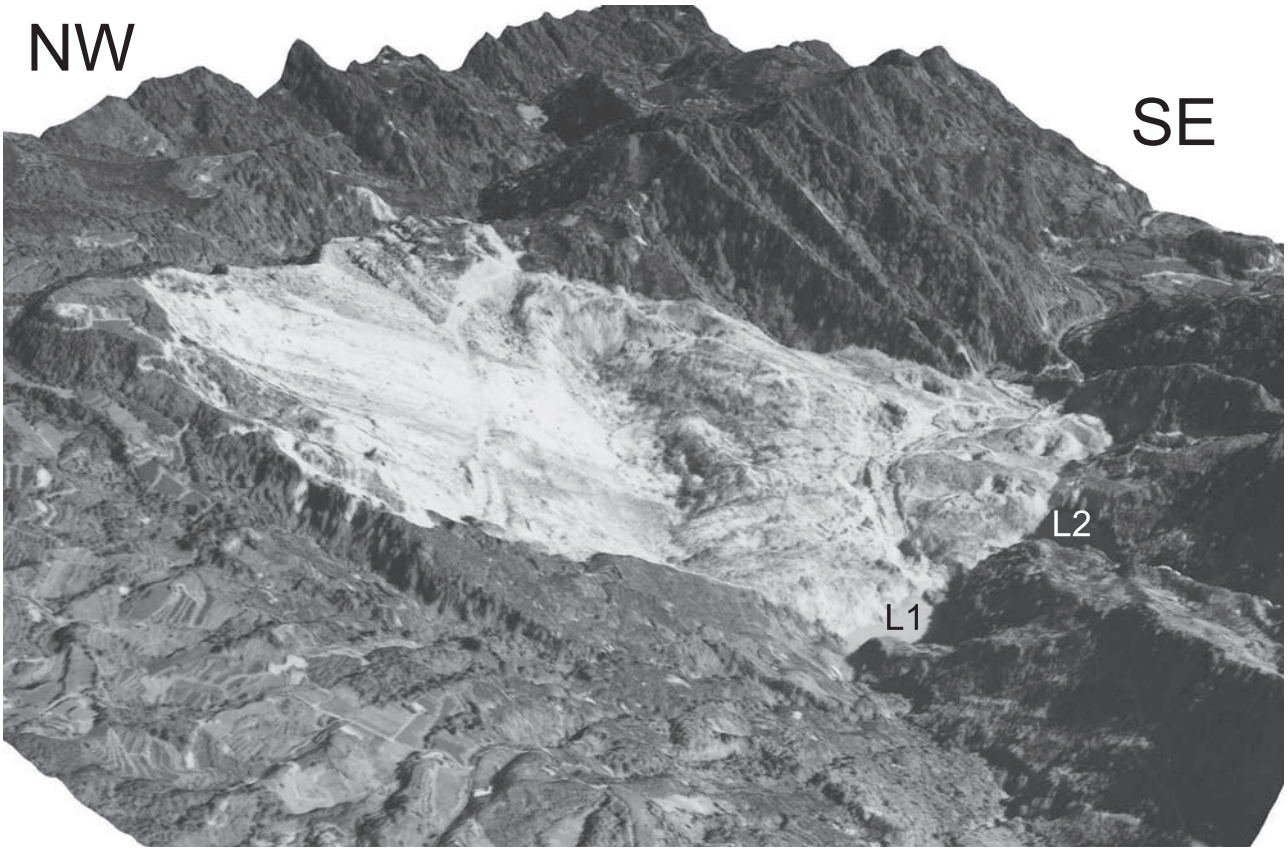

Figure 2. Three-dimensional view of the avalanche zone using an aerial photograph superimposed on a digital elevation model. The sliding area and the debris deposit correspond to the freshly exposed unvegetated zones. L1 and L2 are dammed lakes.

bottom to top in the study area are as follows: the Tanliaoti Shale (TL); the Shihmen Formation (SM); the bottom, middle and top Changhukeng Shale (CHb, CHm, CHt); and the Kueichulin Formation (KC) [*Y. C. Huang*, 1986; *L. C. Wu*, 1986; *C. S. Huang et al.*, 2000, 2002; *Mao et al.*, 2002; *Wang et al.*, 2003a; *Chang et al.*, 2005a].

[14] The Jiufengershan avalanche transported a 42–65 m thick, 1.5 km long rock-and-soil mass on the western limb of the Taanshan syncline (Figure 1) [*Chang et al.*, 2005a]. The landslide deposit accumulated downslope, along the syncline axis. The tilted layers mobilized in the earthquake consisted of surface soils as well as fractured and weathered rocks of the Changhuken Shale (CH). This geologic formation is mainly composed of thick-bedded, muddy sandstones with intercalated thin shale beds of Early to Middle Miocene age [*Y. C. Huang*, 1986; *L. C. Wu*, 1986]. The sliding materials involved the top layers of the CHm member (10–20 m), and the overlying layers of the CHt member (~40 m). The rupture surface was surmised to be located along a weak (partially weathered) stratigraphic layer oriented N36°E, and dipping 21–23°SE.

[15] The displaced mass involved two superposed flatiron remnants that were entirely mobilized during the avalanche [*Chang et al.*, 2005a]. Figure 2 shows an aerial photograph of the avalanche zone, superimposed on a digital elevation model. The sliding area and the debris deposit form a freshly exposed, unvegetated zone. The rupture surface was a triangular plane dipping toward the SE, whereas the debris deposit corresponds to the hummocky topography located downhill. The northern and westward boundaries of the flatirons corresponded, respectively, to an E-W trending valley and to V-shaped notches that limited the tilted layers. These lateral boundaries formed free surfaces that did not restrain sliding.

[16] No important mass movements had occurred in the Jiufengershan area before 1999 and, in particular, erosion at the toe of the flatiron remnants was not observed before the earthquake. Thus, toe erosion did not contribute to the triggering of the landslide. Nevertheless, chemical weathering had affected the upper layers of the flatiron slope, in particular near the valley. The rock-and-soil avalanche was slowed by morphological obstacles in the neighborhood of the Jiutsaihu creek, which was partly filled by avalanche debris deposit. These obstacles correspond to steep NS trending ridges observed in the eastern limb of the Taanshan syncline. They are composed of competent sandstones of the Shihmen formation (SM). Three small lakes formed upstream from the debris deposit, two of which are visible in Figure 2.

[17] The deposit consists of a "chaotic" mixture of small rock fragments and jointed blocks, ranging in size from a few centimeters to more than 20 m in diameter. In particular, intense shearing and fragmentation generated complex facies in which stratification is indistinct. The rock-and-soil avalanche began as a translational slide consisting of large blocks that were rapidly broken to form an avalanche, as the

Table 1. Strength Parameters for Intact and Weathered Rock and for Preexisting Shear Planes[a]

Parameter	Intact Rock	Weathered Rock	Shear Plane
c'_{max} (kPa)	280–960 (4600)	30–40	0
ϕ'_{max} (°)	35.3–36.1 (38)	31.1–34.3	22.9–25.3
c'_{res} (kPa)	30–40 (50)	0–10 (25)	0
ϕ'_{res} (°)	31.4–33.2 (30.8)	28.3–31.1 (27.3)	20.2–23.2

[a]Strength parameters from *Chindao* [2001, 2002]. Here c'_{max} and c'_{res} are the maximum and residual effective cohesions and ϕ'_{max} and ϕ'_{res} are the maximum and residual effective friction angles. The properties of the Changhuken shale close to the surface of rupture are indicated in parenthesis [*Shou and Wang*, 2003].

material was pulverized in transit. The blocks probably split and broke apart along preexisting fractures that are well identified below the surface of rupture. After the earthquake, an elongated depression was observed at the rear of the avalanche deposit.

3. Numerical Model

[18] In this section, we present a numerical model for the earthquake-triggered Jiufengershan avalanche, integrating information from geological, geotechnical, morphological, and seismological data sets. As explained forward, this model shares a certain number of common features with the hypothetical example of a rain-triggered avalanche presented in the companion paper [*Taboada and Estrada*, 2009, section 5]. The main common features between both examples are as follows: (1) the initial geometry and structure of the hillslope granular model defined from a geological cross section across the Taanshan fold (Figure 1); (2) the granular behavior law which is defined from strength parameters of weakly weathered rock; (3) the geometry of the water table within the hillslope, which is parallel to the bedding; (4) the dynamic weakening of the surface of rupture during avalanche triggering; and (5) the mechanical model for simulating both the effect of pore water before the avalanche and the pore pressure release during avalanche triggering. These similarities allow comparison between numerical simulations of an earthquake-triggered avalanche and a rain-triggered avalanche.

[19] However, our primary objective is to study the influences of specific characteristics of the hillslope and the slip surface on the initiation and motion of earthquake-triggered avalanches, which mobilize shallowly dipping layers. These characteristics are, in particular, the strength of rock and soil materials in the bulk, the water table height with respect to the surface of rupture, and the geometry and strength of the surface of separation. In addition, we determine the most plausible strength parameters for both the bulk and the slip surface materials of the Jiufengershan avalanche, from back analysis of the debris morphology (i.e., by comparing avalanche topographic profiles with simulated surface profiles for five cross sections).

3.1. Bulk

[20] This section presents the macroscopic strength parameters of hillslope materials as well as the contact-scale parameters of the corresponding granular materials. The mechanical interactions between particles in the granular model are defined in order to match the strength of rock samples extracted from boreholes. More precisely, macroscopic friction and cohesion are fitted by combining friction, adhesion and bending moment strength at contact scale [*Taboada et al.*, 2006].

3.1.1. Shear Strength of Rock Samples

[21] The physical and mechanical properties of the mobilized sedimentary rocks have been studied by means of classic geotechnical tests [*Chindao*, 2001, 2002; *Shou and Wang*, 2003]. The quasistatic behavior law of rocks and soils was characterized in terms of Mohr-Coulomb rupture envelopes, determined from laboratory shear tests. Several holes were cored in the lateral slopes adjacent to the sliding area (Figure 1) [*Chindao*, 2001, 2002; *J. H. Wu et al.*, 2005]. The rock samples show evidence of physical and chemical weathering visible such as (1) discoloration of the cores along large zones of 0.5–3 m thickness, which show a brownish color that contrasts with the light gray color of intact rock; (2) joints and fractures parallel to the stratification located at regular spacing, ranging from 0.1–1 m; and (3) zones of differing fracture density.

[22] Shales of the Changhukeng formation have heterogeneous mechanical properties and large variations in strength depending on the degree of weathering. Table 1 specifies the ranges of shear strength parameters determined for intact and weathered rock as well as for preexisting shear planes. The range of values for effective cohesion and effective friction are indicated for both maximum and residual strengths. The rock materials and shear planes exhibit contrasting strength parameters; for example, at maximum strength, the cohesion of intact rock is between 1 and 2 orders of magnitude greater than the cohesion of weathered rock. Additionally, maximum friction angles for weathered rock are slightly lower than those for intact rock, but higher than those for shear planes.

3.1.2. Shear Strength of Granular Media

[23] In order to study the influence of rock and soil strengths in the bulk on avalanche triggering and motion, we generated three granular materials with appropriate Mohr-Coulomb behavior laws. These laws aim to represent the average maximum and residual strengths for intact, weathered, and weakly weathered rocks mobilized by the avalanche. The maximum and residual strength parameters for the three granular materials, both at the contacts between particles and at macroscopic scale, are specified in Table 2. For each behavior law, the contact strength is defined in terms of sliding friction coefficient μ_s, rolling friction coefficient μ_r, and tensile strength σ_{ext} at cohesive bonds. In addition, the corresponding strength at macroscopic scale is defined in terms of effective cohesion and effective friction angle.

[24] The selected intact rock (IR) behavior law considers average strength parameters for the low-strength Changhukeng shale. The effective cohesion is low (1 MPa), and the internal friction angle is intermediate to high. The selected strength parameters for weathered rock (WR) are degraded with respect to those selected for intact rock: the effective cohesion is substantially lower and the effective friction angle is slightly lower. These two laws define extreme strength values for the displaced material, which possibly exhibited an intermediate behavior law.

[25] The weakly weathered rock (WWR) strength parameters suppose an intermediate behavior for the bulk. The

Table 2. Contact and Macroscopic Strength Parameters for the Three Granular Materials Considered in the Numerical Simulations and for the Lines That Bound the Granular Models[a]

	Granular Materials			Bounding Lines	
	IR	WR	WWR	DP and FB	SS
Contact Parameters					
σ_{ext} (kPa)	1200	60	100	100	–
σ_{res} (kPa)	100	0	25	0	0
μ_s	0.23, 0.19	0.3	0.3	0.7, 0.5	0.1, 0.2, 0.4
μ_r	0.25	0.06, 0	0.1	0.1	0.1
Macroscopic Parameters					
c'_{max} (kPa)	1000	40	88	70	–
ϕ'_{max} (°)	38	32.5	38.5	35	–
c'_{res} (kPa)	40	0	13	0	0
ϕ'_{res} (°)	32.3	29.5	26.2	26.6	5.7, 11.3, 21.8

[a]Variables the same as in Table 1; IR, intact rock; WR, weathered rock; WWR, weakly weathered rock; DP, dipping plane; FB, frontal backstop; SS, surface of separation. Here σ_{ext} and σ_{res} are the maximum and residual tensile strengths, μ_s and μ_r are the sliding and rolling friction coefficients (maximum and residual values are specified if different),; c'_{max} and c'_{res} are the maximum and residual effective cohesions, and ϕ'_{max} and ϕ'_{res} are the maximum and residual effective friction angles. The residual strength parameters along the SS can take any of the three values that are specified, depending on the numerical simulation.

maximum effective cohesion selected for WWR is about ten times lower than for IR, and twice as high as for WR. In addition, the maximum internal friction angle of WWR is close to that of IR. Thus, the failure envelopes for IR and WWR are roughly parallel but separated vertically.

3.2. Slip Surface

[26] The 2-D granular model is bounded by a set of lines representing the physical boundaries of the rock-and-soil avalanche, which are named as follows (see inset in Figure 1): the dipping plane (DP), the frontal backstop (FB) and the surface of separation (SS). The potential slip surface of the avalanche mainly involves the dipping plane (i.e., the surface of rupture) and the surface of separation. The strength properties along these boundaries exert a major control on initiation and motion of the avalanche.

[27] The dipping plane (DP) corresponds to the potential surface of rupture of the landslide. The maximum and residual friction and cohesion along this interface control incipient sliding of the tilted layers. We make the hypothesis that the surface of rupture was localized along a weakly weathered horizon similar to those observed in the nearby boreholes. These horizons exhibit degraded strength properties as a consequence of physical and chemical weathering processes; the latter were possibly activated by infiltration of rainwater along joints and bedding plane shears formed during the folding of the syncline. Thus, it seems reasonable to suppose that the average strength parameters along the DP are similar to those of weakly weathered rock (Table 2). Note that the selected value for residual strength along the DP supposes cohesionless behavior and an effective friction angle $\phi_{res} = 26.6$, which is higher than the dip angle of tilted layers. In these circumstances, the downslope component of weight of the tilted layers is balanced by the shear stress along the DP and by normal forces applied at the frontal backstop, and an avalanche cannot be triggered even by seismic shaking [*Chang et al.*, 2005b].

[28] We hypothesize that avalanche triggering along a dip slope requires dynamic weakening of the surface of rupture, which reduces the shear strength well below the residual frictional strength [see *Taboada and Estrada*, 2009, section 4.3]. In this scenario, the role of seismic shaking is to generate shearing and frictional heating along the surface of rupture, which, in turn, may induce dynamic weakening and avalanche triggering. In the case of the Jiufengershan avalanche, this hypothesis is supported by some evidence of dynamic-weakening mechanisms such as pressurization of pore fluid and shear melting, observed along some exposed areas of the surface of rupture. First, field observations confirm the existence of abnormally high pore pressures in the basal shear zone: adjacent joints were filled with mud injected from nearby saturated clay layers that experienced fluidization during the avalanche [*Chang et al.*, 2005a]. Second, a thin layer of pseudotachylyte (glass or cryptocrystalline material associated with cataclasites) was observed, in particular, along the upper zone of the surface of rupture. Note that the estimated minimum temperature for pseudotachylyte formation is 1100–1600°C for dry rocks [*Lin et al.*, 2001]. This material was formed by frictional and viscous heating during sliding. Shear melting probably occurred at high shear rates, following other thermal weakening processes that may have operated at submelting temperatures during avalanche motion.

[29] For simplicity, we assume that the shear strength along the dipping plane is "slip weakening" and that the reduction in shear strength is defined by a step function (i.e., the shear strength is constant for slip distances lower than a critical slip distance D_c and drops to zero at this threshold distance). This approximation mimics the sharp (e.g., exponential) decrease in shear strength as a function of slip distance, characteristic of dynamic-weakening mechanisms such as pressurization of a pore fluid. We have set $D_c = 5$ m, which is consistent with slip-weakening distances inferred for rock avalanches that were assumed to be triggered because of pressurization of a pore fluid [e.g., *Chang et al.*, 2005b; *Veveakis et al.*, 2007]. The dynamic behavior of the granular hillslope was also analyzed for other threshold distances (1–10 m); but this parameter only affects the response time of avalanche triggering and does not modify the main results of this study.

[30] The frontal backstop (FB) acts as a support that restrains downslope motion of the tilted layers. This boundary is perpendicular to the DP, and therefore not susceptible to shearing during the avalanche. The shear strength properties of the FB are similar to those of weakly weathered rock, but they have no influence on hillslope behavior.

[31] The surface of separation (SS) is a complex interface along which soil, vegetation, and other sliding materials, are sheared at high velocities. In addition, specific dynamic weakening mechanisms, such as lubrication of the slip surface by liquefied saturated soils, may operate along this interface during avalanche motion [e.g., *Buss and Heim*, 1881; *Hungr*, 2006]. However, in the absence of direct observation of the SS (which is covered by the debris), the origin of weakening mechanisms along this interface remains conjectural. To simplify, we suppose that the average shear strength along this interface is estimated by a single parameter, namely, the angle of sliding friction (i.e., cohesive forces are neglected). The role of this parameter on

avalanche motion is analyzed by testing three different values (Table 2).

3.3. Pore Water Pressure

[32] The earthquake occurred during the rainy season and, as will be recalled in section 4.1, the water table was reasoned to be located well above the sliding plane [*Chang et al.*, 2005a]. Aerial photographs taken three days after the earthquake showed water seepage and small springs, located near folded and faulted rocks observed on the surface of rupture. These observations suggest that groundwater was flowing along interlayered permeable rocks and preexisting joints.

[33] We assume that the water table was located at a constant height above the potential surface of rupture. This simplification allows us to test the effect of the water table height h_w on the stability of the dip slope, under dynamic (seismic shaking) conditions. For slow flow rates, the effect of groundwater flow on particles located below the water table may be simulated by the combined effect of buoyancy and seepage forces [see *Taboada and Estrada*, 2009, sections 3.4 and 5.4]; the resultant force may be defined by the product of the pore pressure gradient and the particle volume.

[34] We suppose that pore pressure in the bulk is negligible once the avalanche is triggered and dilatant deformation initiates. This condition is introduced in the numerical approach by deactivating pore pressure forces, once the particle has moved a distance greater than a critical distance D_c (e.g., 5 m). Note that the same critical distance is used to vanish frictional strength along the surface of rupture and to release pore pressure at particle scale. Thus, the pore pressure release coincides with slip weakening and avalanche triggering.

3.4. Earthquake Data

[35] Earthquake shaking is introduced in the model by imposing a velocity field calculated from strong motion acceleration records of the Chi-Chi (1999) earthquake. A large number of acceleration records with absolute timing was gathered during the earthquake by the Central Weather Bureau (CWB) of Taiwan from digital strong motion instruments at free-field sites [*Shin et al.*, 2000; *Lee et al.*, 2001]. Strong motion records are defined by three components measured along the east-west, north-south, and vertical upward directions. Seismic acceleration records from nearby stations are usually considered as the most reliable for geotechnical applications [*Crespellani et al.*, 2003]. We selected records from station TCU071, located at 5.7 km from the landslide. For simplicity, we neglected ground motion amplifications, which probably occurred at the mountain crest in the low-frequency domain [*Havenith et al.*, 2003]. We also tested records from two other nearby stations (TCU072, TCU089) in order to determine the sensitivity of results to seismic input.

[36] Figure 3 shows the components of the acceleration, velocity, and displacements registered in station TCU071 in two perpendicular directions (pointing upward and parallel to the dip slope). The records cover a preevent interval of 20 s, followed by ~137.5 s, which includes the earthquake signal. The ''uncorrected'' strong motion acceleration records are filtered using conventional seismological algo-

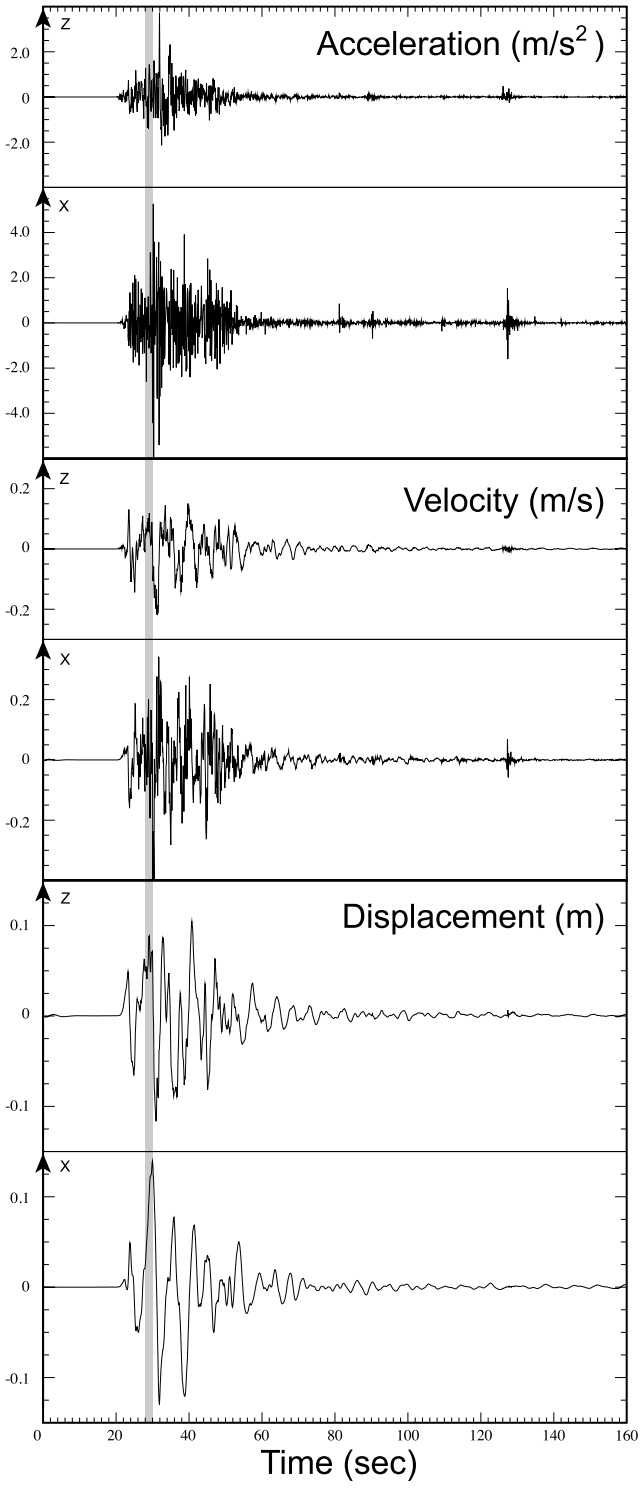

Figure 3. Components of the acceleration, velocity, and displacements registered in station TCU071 during the 1999 Chi-Chi earthquake in two perpendicular directions (pointing upward and parallel to the dip slope). The station is located at 5.7 km from the avalanche. The vertical shaded band indicates estimated time of avalanche triggering for the numerical model that uses the intermediate behavior law (i.e., weakly weathered rock). Here h_w = 30 m (Figures 4e, 5, and 6).

rithms including baseline corrections and band-pass filtering with Butterworth filter cut-off frequencies (>0.2 and <20 Hz). This data processing is done in order to prevent errors resulting from background noise, instrument natural response [*Kramer*, 1996; *Boore*, 2001; *Crespellani et al.*, 2003], and residual displacement [*Boore*, 2001].

[37] In the numerical simulations, the line segments that bound the granular assembly are velocity controlled: they move according to the velocity record obtained from the integration of the seismic acceleration record (Figure 3). The velocity components are calculated from the corrected accelerations in a reference frame perpendicular to the strike of the granular layers. The velocity component parallel to the strike is neglected in this two dimensional analysis.

4. Simulation Results

[38] The dynamic behavior of the granular hillslope was analyzed under different hypotheses concerning the composition of geological layers, water table height, and shear strength along the boundary. We used strong motion records from station TCU071. Nevertheless, similar results are obtained using records from two other nearby stations. Strength parameters are estimated by comparing avalanche topographic profiles with simulated surface profiles for 5 cross sections (Figure 1). Animations S1–S21 illustrate the triggering and motion of the avalanche for all numerical simulations are available in the auxiliary material.[1]

4.1. Water Table and Bulk Strength

[39] The water table height h_w above the sliding plane was estimated from three boreholes drilled next to the sliding area (i.e., at a distance of ~50 m), in materials that did not fail (Figure 1) [*Chindao*, 2001]. Values for h_w range between 20 m and 40 m, and an average value of 30 m was selected as representative of the groundwater conditions present during the earthquake. Measurements of water table height were done in August (2001) during the rainy season, under climatic conditions similar to those preceding the avalanche. However, the water table heights are probably lower than before the earthquake as a consequence of water flow toward the new free boundary (i.e., the vacated zone).

[40] The mechanical behavior of the granular model was analyzed for different water table heights at intervals of 10 m. For the intact rock behavior law, the avalanche is triggered by the earthquake only if the water table height $h_w \geq 40$ m. For the intermediate and weathered rock rheologies, the avalanche-triggering threshold is given, respectively, by $h_w = 30$ m, and $h_w = 0$ m. These thresholds vary slightly when strong motion records from other nearby stations are used in the simulations. Nevertheless, the dynamic behavior of the avalanche is quite similar once it has been triggered, independently of the specific seismic record.

[41] The shear strength of the granular layers has a major influence on the dynamic behavior of the dip slope and on the deformation pattern of the avalanche deposit. Figures 4a–4c show the morphology and the structure of the granular deposits obtained for the three granular materials that are presented in Table 2. The geometry of the slip surface is the same for the three models. Additionally, the geometry of the surface of separation (SS) is defined by a linear segment with rising (negative) slope (i.e., positive slopes dip in the same direction as the hillslope). This geometry is a simplified representation of the topographic profile of section D, before the avalanche (Figure 1). The dashed magenta and solid blue profiles correspond to the topographic profiles of this section before and after the avalanche. In the three simulations, the friction coefficient at the SS and the water table height are fixed, respectively, at $\mu_{SS} = 0.2$, and $h_w = 40$ m.

[42] For intact rock, the granular layers are much shortened and compressed during the avalanche (Figure 4a). The morphology of the avalanche granular deposit shows two distinct parts: a downhill zone characterized by a concave down profile and an uphill zone characterized by a step profile. The downhill zone shows a sequence of disharmonic folds located above a major décollement. These folds result from intense shearing and compression of the layers occurring predominantly when the sliding material reaches the foot of the dip slope. The deformation mechanism involves buckling and shortening as explained in section 4.3. The step profile observed uphill is defined by granular layers subjected to translational motion parallel to stratification. These layers were weakly deformed during the avalanche owing to their strength.

[43] For weakly weathered rock (intermediate behavior law, Table 2), the granular layers in the deposit also show intense folding and shearing resulting from compressional stresses (Figure 4b). The overall morphology is concave down, showing small antiforms located above anticlinal folds. A large overturned fold is observed near the tip of the granular deposit. The overturned limb results from shearing along the surface of separation. The head of the granular deposit shows a smoother morphology than in the previous situation. The top and the tip of the displaced material fit the topographic extension of profile D (solid blue line) quite well.

[44] Compressional deformation is more intense for weathered rock than for weakly weathered or intact rock; in particular, disharmonic folds on weathered rock have larger amplitudes and shorter wavelengths (Figure 4c). In contrast, the morphology of the granular deposit for weathered rock is smoother: it has a triangular shape as in a sand pile, with very gentle slopes. This morphology results from the absence of residual cohesion in the contact law (Table 2). The tip of the avalanche deposit is shifted toward the right, indicating that the avalanche propagated further than for the stronger granular materials. The layers located at the rear of the granular deposit underwent intense shortening owing to their low strength.

[45] The deformation mechanism in weathered rocks involves diffusion: particles from adjacent layers mix during the avalanche as observed at the rear of the granular deposit (e.g., green intermediate layer, Figure 4c). This mechanism, also known as dispersive inflation, has been described in large sturzstroms [*Pollet and Schneider*, 2004]. It results from dynamic disintegration processes in dilatant granular flows, which may jumble the stratification. Note that the stratification is often indistinct in avalanche debris deposits as a consequence of dynamic disintegration processes.

[1] Auxiliary materials are available in the HTML. doi:10.1029/2008JF001075.

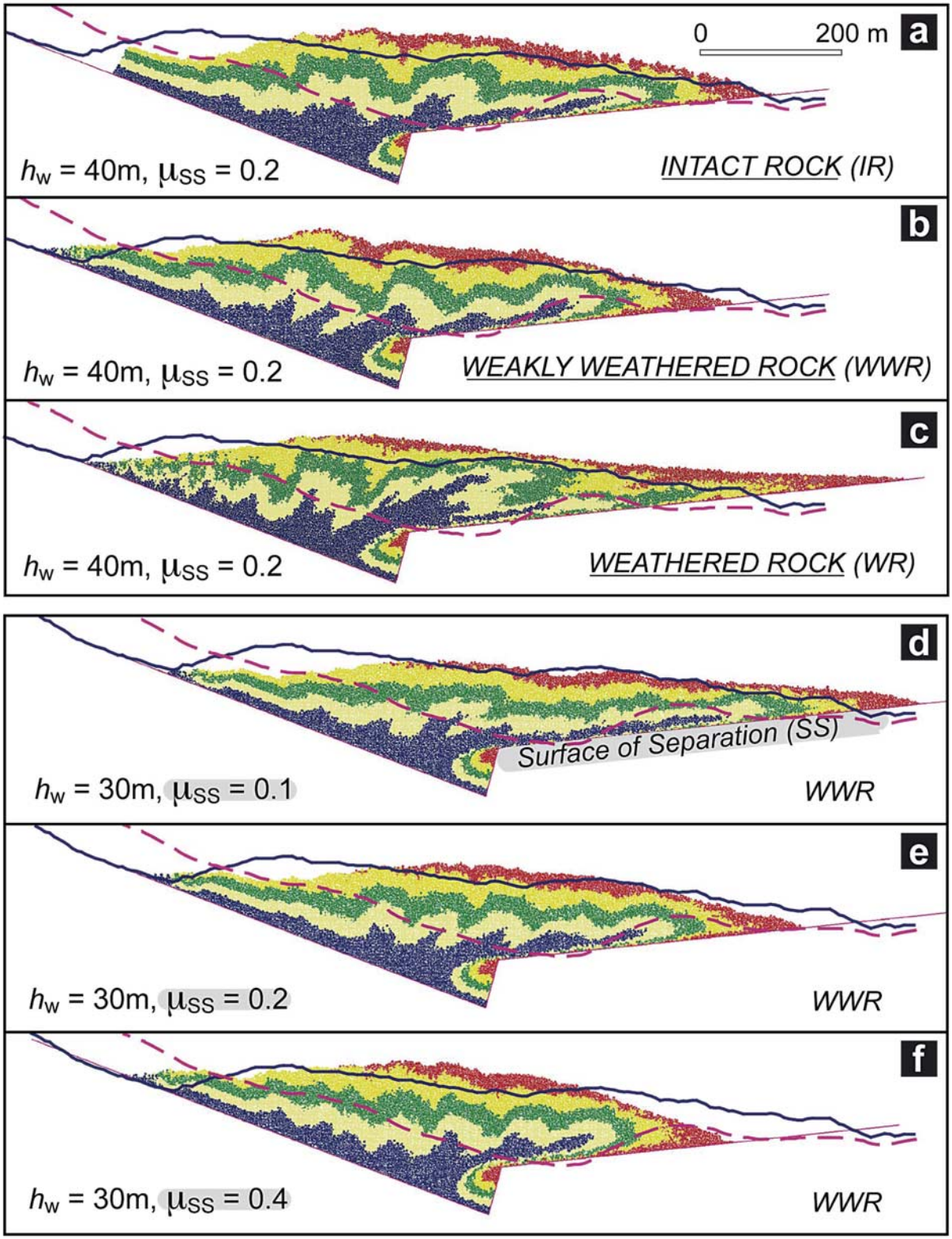

Figure 4. Numerical simulation of the granular deposit obtained for (a–c) the three behavior laws in Table 2 and (d–f) three shear strengths at the surface of separation. The dashed magenta and solid blue profiles correspond to the morphology of section D before and after the avalanche (Figure 1). Here h_w is the water table height above the DP and μ_{SS} is the friction coefficient at the SS.

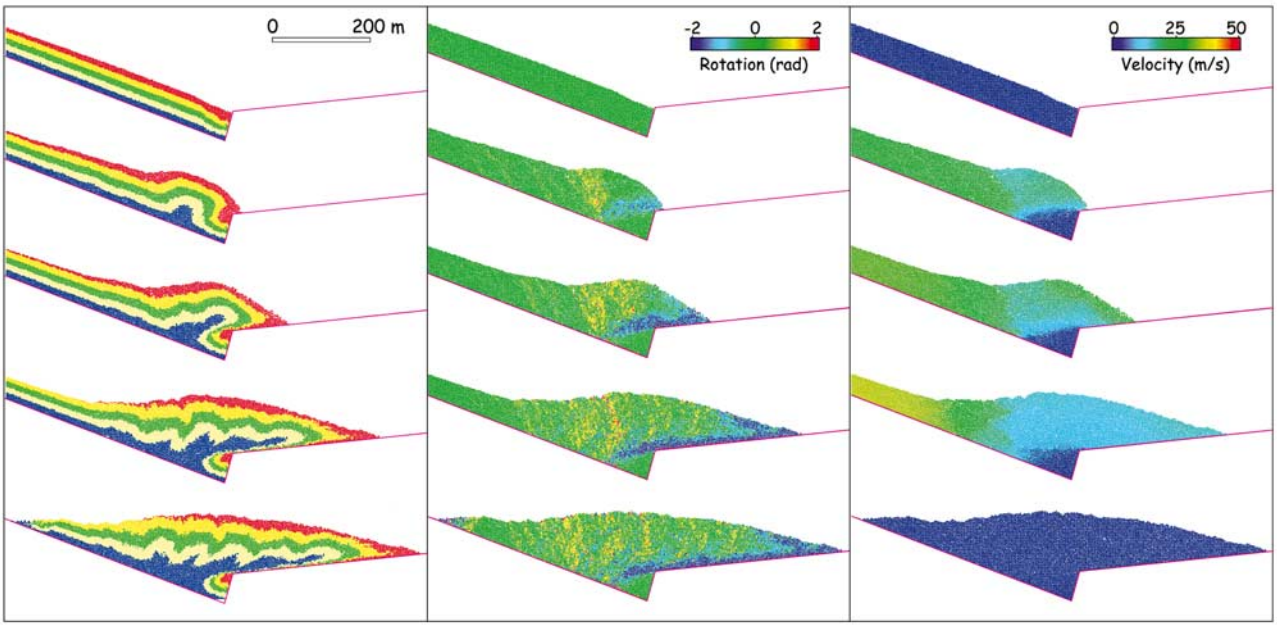

Figure 5. Close-ups showing the displacement, rotation, and velocity fields at five stages during the avalanche (same geometry and parameters as in Figure 4e, i.e., WWR, h_w = 30 m, μ_{SS} = 0.2, rotation scale in radians, positive is counterclockwise).

4.2. Shear Strength at the Surface of Separation

[46] The motion of the avalanche is largely controlled by the shear strength at the surface of separation (SS). Figures 4d–4f illustrate the influence of the shear strength at the SS on the morphology and the structure of the granular deposit. In these simulations, the granular material behaves as weakly weathered rock and the water table height h_w is fixed at 30 m. The friction coefficient μ_{SS} at the SS in Figures 4d–4f is fixed, respectively, at 0.1, 0.2 and 0.4 (the corresponding friction angles are specified in Table 2). The topographic profiles across section D (Figure 1) are also indicated.

[47] The morphology and structure of the granular deposit are highly dependent on the friction coefficient μ_{SS} along the surface of separation. Several features are sensitive to variations in the friction coefficient. Firstly, as the friction coefficient decreases, the granular deposit is longer and thinner, the runout distance increases, and the mean surface slope is gentler. For the lowest friction value (μ_{SS} = 0.1) the avalanche advances ~600 m over the SS, whereas for the highest friction value (μ_{SS} = 0.4) it only advances ~325 m. Secondly, as the friction coefficient decreases, the shortening and folding of the geological layers is less intense (see Animations S1–S21 in auxiliary material); for low friction values, the materials in the foot of the avalanche can be pushed forward more easily by the main body of the avalanche located uphill. Finally, as the friction coefficient decreases, the top of the granular deposit is slightly shifted downhill.

[48] The effective friction coefficient at the SS cannot be measured either in the field or in the laboratory, but may be determined from a back analysis by comparing the avalanche topographic profile with the simulated surface profile. Among the strength values specified in Table 2, the best fit between the topographic and the simulated surface profiles is obtained for the intermediate behavior law (i.e., WWR), by using the following set of parameters: h_w = 30 m, and μ_{SS} = 0.2 (i.e., Figure 4e). The selected value (μ_{SS} = 0.2) is much lower than the friction coefficient of weathered rock (Table 1), and it is closer to the residual friction coefficient for saturated fine-grained soils such as clays [*Bardet*, 1997]. This result suggests that the friction coefficient μ_{SS} is controlled by the rheology of low-strength unconsolidated soils that mantled the SS. Lubrication of the basal shear zone by liquefied saturated soils dragged from the slide path may have contributed to the reduction of friction, therefore increasing the runout of the avalanche [e.g., *Buss and Heim*, 1881; *Hungr and Evans*, 2004].

[49] The travel angle (α) of the Jiufengershan avalanche is calculated from the following relation:

$$\tan \alpha = \mu_{AP} = H_{CT}/L_{CT} \cong 0.22, \quad (1)$$

where μ_{AP} is the apparent friction coefficient, H_{CT} is the difference in elevation between the crown and the tip of the landslide, and L_{CT} is the horizontal distance between the crown and the tip, measured at the center line of the landslide [*Campbell et al.*, 1995; *Cruden and Varnes*, 1996].

[50] The estimated value for μ_{AP} is very close to the mean trendline behavior determined for mobile sturzstroms with similar volumes [*Hsü*, 1975; *Collins and Melosh*, 2003]. Low values for μ_{AP} are characteristic of long-runout landslides with large volumes. Note that the runout distance is mainly controlled by the friction coefficients of both the slip surface and the bulk, which are true mechanical parameters, different from the apparent friction μ_{AP}.

4.3. Avalanche Kinematics and Deformation

[51] The avalanche process is studied by analyzing the kinematic parameters and deformation of the destabilized dipping layers. Figure 5 shows the deformed granular layers

as well as the rotation and velocity of the granular model, at 5 stages from the initial to the final state (see Animations S1–S21 in auxiliary material). The simulation parameters are the same as in Figure 4e. The rotation of particles is measured in radians (positive counterclockwise).

[52] In our simulation, the triggering of the granular avalanche occurs at the beginning of the strong motion record, roughly between 8 and 10 s after the first wave arrival (i.e., shaded band in Figure 3). Thus, seismic shaking persists almost during the entire motion phase of the granular avalanche, which lasts ~40 s.

[53] The triggering is associated with a pop-up structure observed at the foot of the dip slope. This structure is bounded by two conjugated shear zones that initiate from a common point located at the surface of rupture. During incipient pop-up formation, the velocity of particles located upslope is ~1 m/s, indicating that the surface of rupture is sheared as downslope motion begins. The pop-up is progressively deformed into an overturned fold, which overrides the surface of separation along a major synthetic décollement. Particles in the shear zone show large clockwise rotations that are consistent with the shear sense.

[54] The granular layers that slide downslope are subsequently folded and disrupted as they reach the toe of the dip slope. The folding pattern is given by a sequence of disharmonic folds that are transported within the foot of the avalanche. The foot of the displaced mass forms a wedge that is pushed forward as deformed rocks accrete at its rear.

[55] In contrast to the folding pattern, the profile of the wedge is relatively smooth as a result of particle rearrangements and shallow granular flow (in the tip of the avalanche). Nevertheless, small transverse ridges are observed, in particular, above the newly formed folds. The average slope of the wedge corresponds to a critical stability angle that depends on frictional strength properties.

[56] Anticlinal folds are bounded by antithetic shear bands that are formed simultaneously with folding. Particles in these diffuse shear zones show predominantly positive (anticlockwise) rotations (Figure 5 (middle)). The main shear zones observed in the wedge at the final stage are indicated in Figure 6d. Antithetic shears are interpreted as steep angle reverse faults, which initiate near the footslope. As the granular wedge advances, the lower part of the shear zones is overturned as a consequence of basal shearing. The head of the granular deposit is less deformed than the wedge, yet incipient antithetic shears are observed.

[57] The deformation process can be analyzed in terms of velocity variations within the granular system. The downslope translational motion is characterized by extremely rapid velocities that reach ~35 m/s (125 km/h). These velocities contrast with those observed in the wedge, which are roughly 50% lower. The wedge is, on average, twice as thick as the original granular layers, and consequently, it advances at a lower velocity. The average velocity of the particles in the wedge at any given time is relatively homogeneous indicating low deformation during its mobilization.

[58] The granular layers are folded at the zone located between the translational slide and the wedge, where the velocity gradients are the largest. This zone shows compressive flow, since the particles are slowed as the layers are folded and accreted to the wedge. The geometry of the slip surface is concave up showing a sharp change in slope at its lowest point (Figure 6d). The concavity of the slip surface promotes compressive flow, as observed in slow surface processes such as glaciers [*Summerfield*, 1994].

[59] The motion of the avalanche is controlled by the balance between available mechanical energy and energy dissipation. The mechanical energy is the sum of the potential energy of granular layers located upslope and the kinetic energy of the granular system. Energy dissipation is due to frictional interactions, plastic deformation, and inelastic collisions. In the initial stage of avalanche motion, the dissipation is low and potential energy is mainly converted into kinetic energy. At this stage the granular system accelerates. As the granular wedge grows and advances along the SS, energy dissipation increases and the kinetic energy diminishes. Thus, the average velocity of the wedge decreases as the top of the avalanche approaches the zone of accumulation.

4.4. Geometry of the Surface of Separation

[60] The simulation of five cross sections across the Jiufengershan avalanche illustrates the strong influence of the slope of the surface of separation on the folding pattern and the runout distance (Figures 1 and 6). For each cross section, the selected geometry of the SS corresponds to a simplified topographic profile of the original ground surface before the avalanche. The dashed magenta and solid blue profiles indicate the topography of the sections before and after the avalanche, respectively. The main shear zones formed during avalanche motion are also indicated (synthetic and antithetic shears in black and red, and extensional faults in blue).

[61] The simulation parameters are the same as in Figures 4e and 5 (weakly weathered rock, h_w = 30 m, and μ_{SS} = 0.2). These parameters were selected among the strength parameters in Table 2, in order to obtain the best fit between the topography and the simulated surface profiles. The surface profiles, as well as the overall extension of the simulated deposits match reasonably well the topographic profiles across the avalanche debris deposit, given the uncertainties and simplifications that are inherent in the numerical model. The error between simulated and topographic profiles was estimated calculating the relative mismatch between the two; namely, the area located in between the two profiles divided by the area of the debris deposit. The estimated errors (in percentage) for the five cross sections are between 8 and 15%, and they are randomly distributed along the profiles.

[62] The longest-runout distance is observed for the SS dipping downslope (Figure 6a), where the weight component in the direction of motion is maximum. The SS is given by a 600 m linear segment that dips 6° toward the toe of the avalanche. The linear segment is connected to a ramp dipping −30°, which confines the avalanche. The granular deposit shows compressional deformation characterized by gentle disharmonic folds and a recumbent fold near the toe of the granular deposit. The average slope of the granular wedge is slightly steeper than the surface of separation. Note that the granular deposit for a downslope dipping SS is much thinner and longer than for a horizontal or upslope dipping SS.

[63] Extensional granular flow is observed in the final stage of avalanche motion for downslope dipping SS

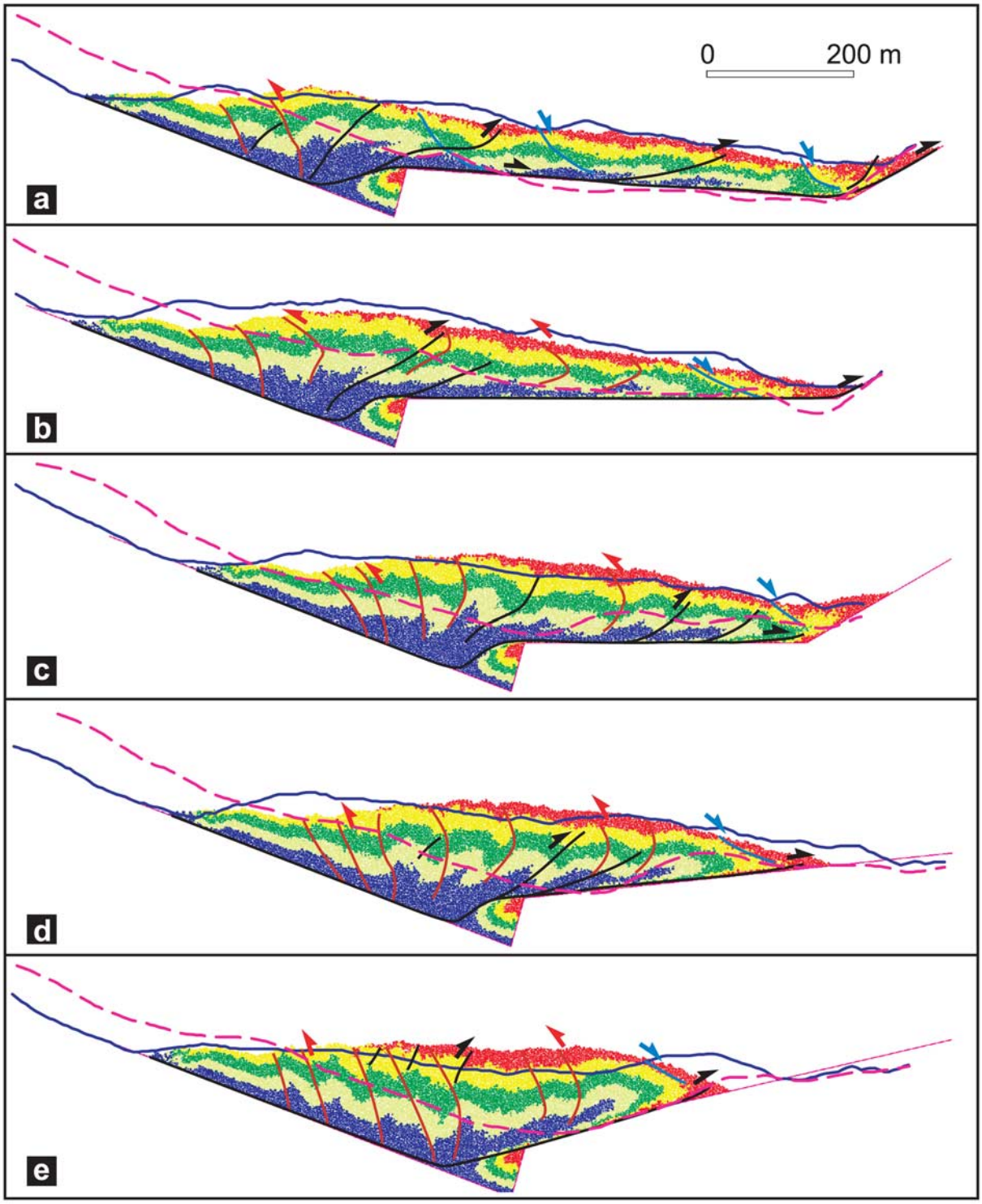

Figure 6. Numerical simulation of the granular deposit for the five cross sections in Figure 1 (same parameters as in Figure 4e, i.e., WWR, h_w = 30 m, μ_{SS} = 0.2). The dashed magenta and solid blue profiles indicate the topography of the sections before and after the avalanche. Synthetic and antithetic shears are indicated in black and red, and extensional faults are indicated in blue.

profiles (see auxiliary material). Local extension results from specific mechanical conditions related to the geometry of the slip surface: granular material tends to be blocked at the toe of the dip slope while it continues to flow downward over the SS. The transition area between these two zones shows synthetic normal shear bands (in blue) that cut across the previously folded beds. The particle rotation along these shear bands is clockwise (negative) as shown in the corresponding animation file. This deformation regime indicates that the foot of the avalanche is ''stretched out'' down the SS.

[64] Extensional flow is favored by the convex up geometry of the slip surface at the toe of the dip slope. Convexity is more prominent when the SS is dipping downslope. Note that, in our numerical model, the geometry of the slip surface is fixed. Conversely, in natural conditions, the displaced mass might drag underlying material and smooth the convex up geometry, reducing extensional flow.

[65] The runout distance and the length of the granular deposit are shorter for horizontal than for the downdipping SS. The geometry of the SS in Figures 6b and 6c is characterized by a horizontal flat and a ramp. The flat segments measure, respectively, 600 m and 400 m. For the longer flat, the tip of the avalanche propagates slightly beyond the ramp. In this situation, the downstream surface profile of the granular wedge is linear, dipping $\sim 9.5^\circ$. For the shorter flat, the avalanche is slowed down as its tip overrides the ramp along ~ 140 m. Thus, shortening and folding are more pronounced. The morphology of the wedge is convex up showing two small concave zones at the front and at the rear of the debris.

[66] Avalanches propagating over a SS dipping upslope generate thicker and shorter granular deposits (Figures 6d and 6e). The SS in Figure 6e is composed of two linear segments dipping, respectively, -17° and -13° (Figure 6d was described in previous sections). For the steepest SS (Figure 6e), the runout distance decreases and compressional deformation migrates toward the rear of the granular deposit. In this situation, antithetic shear bands responsible for thickening are particularly well developed. No extensional flow is observed in cross sections with an upslope dipping SS, since the geometry of the slip surface at the toe of the dip slope is concave up.

4.5. Contact Forces During Avalanche Triggering

[67] Earthquake shaking weakens progressively the granular material inducing shear rupture and a redistribution of contact forces. To illustrate this behavior we show the contact forces near the footslope before the earthquake and during the avalanche-triggering phase (Figure 7).

[68] Contact forces in a granular material organize spontaneously into two imbricated nets known as the strong and the weak networks [*Radjaï et al.*, 1998]. The strong network is characterized by chains of forces whose magnitudes are above the average. These chains follow zigzag trajectories and they are interconnected through bifurcations and arches [*Taboada et al.*, 2005a, 2005b]. In the bulk, they are roughly parallel to the principal compressional stress σ_1. Conversely, the weak network is composed of contact forces whose magnitudes are less than the average, which provide lateral support to the strong chains. The isotropic stress is resisted by both networks while the deviatoric stress is mainly resisted by the strong network.

[69] At the initial state, contact forces applied along the lateral boundaries restrain sliding motion and ensure the stability of the hillslope (Figure 7a). Shear forces applied at the DP and normal forces applied at the FB both contribute to resist the downslope weight component. The magnitudes of contact forces increase progressively with the depth of overburden and toward the frontal backstop. In the bulk, the chains of strong forces are oriented downslope, at a steeper angle than the DP. Near the lateral boundaries, they are deflected and become perpendicular to the DP and the FB.

[70] Avalanche triggering is characterized by a highly perturbed stress pattern due to shearing along the basal décollement (Figure 7b). At this stage, the thickness of the granular layers has increased slightly, indicating the onset of the shortening and failure of the slope. The contact forces show the following features that are characteristic of the failure process: (1) The chains of strong forces (indicating σ_1) are, on average, parallel to the dip slope. (2) The normal forces in the chains are very high, in particular, in the bottom layers. (3) The shear resistance forces along the basal décollement are very low because of loss of cohesive bonds and dynamic weakening of line-disk contacts.

[71] The incipient motion of the tilted granular layers corresponds to a translational slide whose downslope movement is controlled by frictional strength. Subsequently, the shear strength along the surface of rupture appears to drop to zero as frictional shearing induces dynamic weakening. In these conditions, the granular hillslope leans progressively against the frontal backstop, which supports the components of the weight and of seismic accelerations that are parallel to the dip slope. These force components increase downslope as they are proportional to the rock mass located uphill. Thus, shear failure and buckling must occur near the footslope where the magnitude of normal contact forces is the greatest.

5. Summary and Discussion

[72] The earthquake-triggered Jiufengershan rock-and-soil avalanche was simulated using an original approach based on a discrete element method termed Contact Dynamics. This approach is suitable for the analysis of complex surface processes involving cohesive materials subjected to seismic shaking. The dynamic behavior of the granular hillslope was analyzed under different assumptions concerning the composition of the geological layers, the water table height, and the shear strength at the boundaries. We summarize and discuss the main results of this study and their implications in other fields such as paleoseismology.

5.1. Mechanical Processes During Avalanche Triggering and Motion

[73] We assume that earthquake triggering of an avalanche mobilizing shallowly dipping layers in a slope is conditioned by dynamic weakening mechanisms, which may drastically reduce shear strength along the surface of rupture. In this scenario, the role of seismic shaking is to generate inertial forces in the bulk, which, in turn, may induce shearing, frictional heating, and dynamic weakening of the surface of rupture. For simplicity, we assume that shear strength along the surface of rupture is slip weakening and that reduction in shear strength is defined by a step function (i.e., shear strength is constant for slip distances lower than a critical slip distance and drops to zero at this threshold distance).

[74] We identified the following principal mechanical processes that affect the sliding mass:

[75] 1. The incipient deformation forms a pop-up structure observed at the foot of the dip slope. This structure results from high compressional stresses oriented downslope that

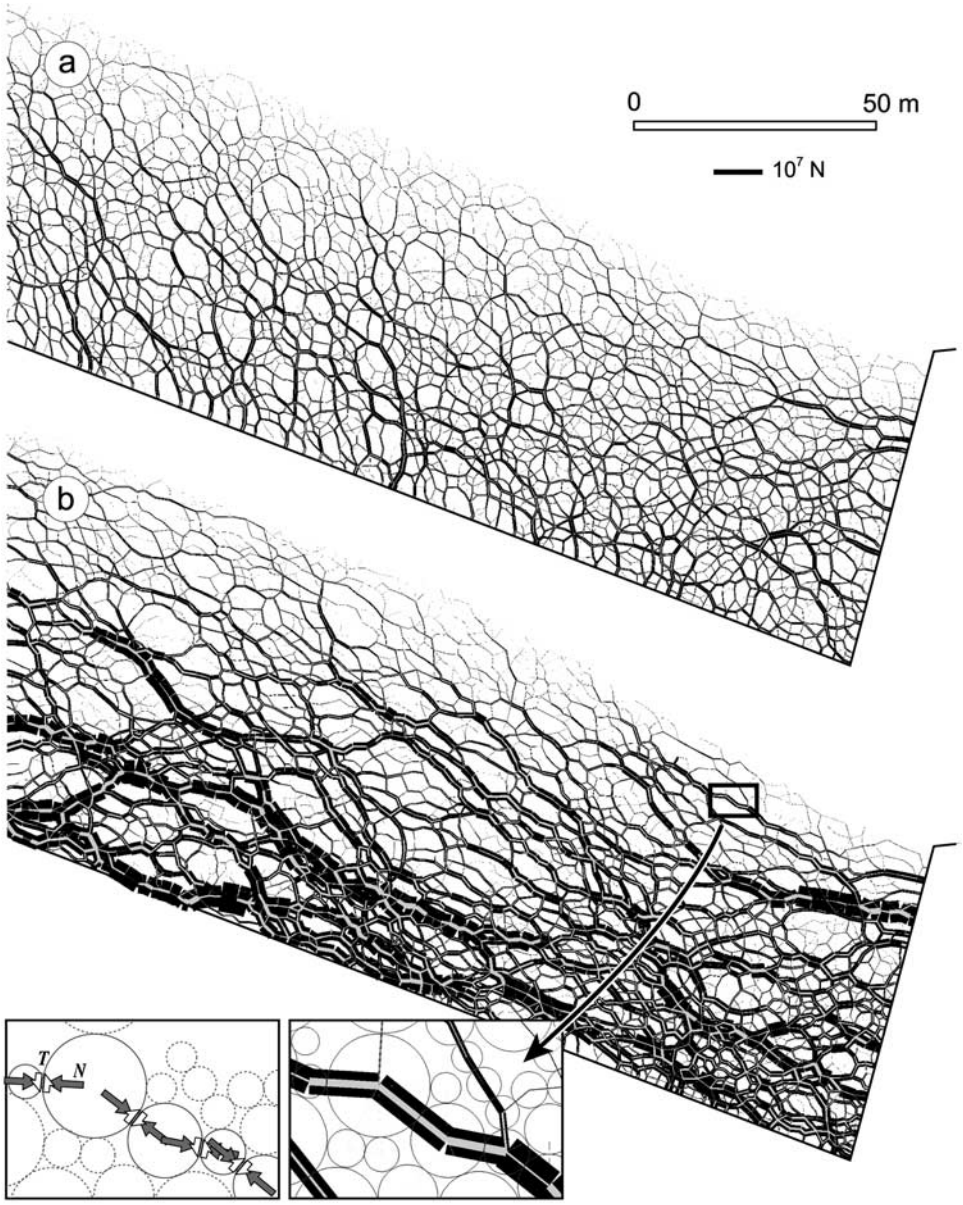

Figure 7. Contact forces near the toe of the dip slope (a) before the earthquake and (b) during avalanche triggering. The normal and shear contact forces are illustrated by rectangles connecting particle centers (for clarity, the disks are not shown). The simulation parameters are the same as in Figure 4e (i.e., WWR and h_w = 30 m). The width of each rectangle is proportional to the magnitude of the contact force according to the scale indicated on the top-right corner. The normal forces N are in black, whereas the shear forces T are in light gray. The blow-up in the bottom-left corner shows contact forces and particles in a small rectangular zone.

concentrate in the footslope area as the surface of rupture is sheared.

[76] 2. As the avalanche propagates, the pop-up is progressively deformed into an overturned fold, which overrides the surface of separation along a major synthetic décollement level.

[77] 3. Simultaneously, the uphill granular layers slide at high velocity (e.g., 125 km/h) and are subsequently folded and disrupted as they reach the footslope.

[78] 4. The foot of the avalanche forms a wedge that is pushed forward as deformed rocks accrete at its rear.

[79] These results provide new insights into the complex deformation mechanisms involved in rock-and-soil avalanches, which are not chaotic as inferred frequently from field observations [e.g., *Pollet and Schneider*, 2004]. Our discrete element approach is well adapted to model processes involving very large strains and diffusive behavior, in which the stratification may be indistinct. In particular, numerical models are useful to identify and interpret mesoscopic-scale structures in the debris deposit such as folds and shear bands; these structures are otherwise difficult to observe in the field because of dynamic disintegration processes.

5.2. Morphology and Structure of the Granular Deposit

[80] The morphology and deformation of simulated deposits are highly dependent on the strengths of the granular layers. The granular deposits show compressional deformation characterized by disharmonic folds, antithetic shear bands, and a recumbent fold in the toe of the deposit. Compressional deformation is more intense for weathered rock than for weakly weathered or intact rock; in particular, disharmonic folds in the weathered rock deposit have larger amplitudes and shorter wavelengths. The weathered rock debris shows a smoother and gentler surface profile, and a longer-runout distance than the deposits composed of stronger materials.

[81] The geometry and frictional strength of the surface of separation (SS) also influence the deformation regime. For example, extensional granular flow is observed during the final stage of avalanche motion when the SS dips downslope. Local extensional flow is favored by the convex up geometry of the slip surface at the toe of the dip slope. In addition, as the frictional strength of the SS decreases, the runout distance increases, and the shortening and folding of the geological layers become less intense.

5.3. Simulation of Cross Sections

[82] The strength properties of the bulk and the slip surface are determined from a back analysis, by comparing the avalanche topographic profiles with the simulated surface profiles for five cross sections. The cross sections differ in the geometry of the surface of separation (SS), which may be horizontal, updipping, or downdipping. The best fit between the topography and simulated profiles is obtained for weakly weathered rock, a water table height $h_w = 30$ m, and a friction coefficient at the SS $\mu_{SS} = 0.2$. Our numerical results are supported by the overall similarity between the observed debris deposit and the simulated granular deposit.

[83] The friction coefficient at the SS cannot be measured either in the field or in the laboratory. This parameter quantifies the average shear resistance along this complex interface in which soil, vegetation, and other sliding materials interact at high velocities. The abnormally low friction value obtained for μ_{SS} may result from lubrication of the basal shear zone induced by saturated soils dragged from the slide path [e.g. *Buss and Heim*, 1881; *Hungr and Evans*, 2004]. Nevertheless, a detailed study of materials and structures along the surface of separation is necessary in order to identify the physical processes that controlled its shear strength.

5.4. Use of Avalanches for Paleoseismic Analysis

[84] One of the major problems in paleoseismic analysis is to show whether an avalanche was triggered by earthquake shaking [e.g., *Jibson*, 1996]. However, our results suggest that the determination of a paleoavalanche trigger cannot be done from the sole observation of the debris deposit.

[85] It appears that the dynamic behavior of earthquake- and rain-triggered avalanches is very similar, once the instability has been triggered. In particular, seismic shaking does not appear to induce abnormally long-runout distances as suggested in some previous studies [e.g., *Solonenko*, 1977]. These assertions are motivated by the comparison between two equivalent models subjected either to seismic shaking or to a rising water table. As explained in section 3, the granular model presented in Figure 6b has the same geometrical configuration and rheology as the rain-triggered avalanche presented in the companion paper [*Taboada and Estrada*, 2009]. The morphology and structure of the granular deposits are very similar in both situations [see *Taboada and Estrada*, 2009, Figure 13]. Nevertheless, the rain-triggered avalanche is slightly less disrupted and its runout distance is slightly shorter (i.e., the tip of the avalanche is located before the ramp).

[86] The low influence of seismic shaking on avalanche motion is presumably related to particle sliding velocities, which are 1–2 orders of magnitude higher than seismic shaking velocities (Figures 3 and 5). Thus, seismic shaking can be viewed as a random high-frequency noise that has low influence on the deformation mechanisms. The detailed analysis of the triggering phase is possibly one of the clues to distinguish earthquake- from rain-triggered avalanches, yet uncertainties on the initial configuration of the hillslope will always exist.

5.5. Limitations and Perspectives

[87] Ground motion amplifications were neglected in the present study in order to simplify the analysis. However, many landslides triggered by the Chi-Chi earthquake propagated from the hillcrests and remained confined to the hillslopes, thus reflecting topographic amplification of seismic waves close to the hillcrests [e.g., *Dadson et al.*, 2004]. Therefore, seismic wave amplifications, which possibly occurred in the Jiufengershan hillslope, may have promoted the triggering of the avalanche, yet they likely had little effect on avalanche motion. Note that simulation results were similar using strong motion records from three nearby stations; as previously mentioned, the deformation pattern is not sensitive to the seismic input, once the avalanche has been triggered. More numerical analyses should be done to determine the precise effect of ground motion amplifications on the avalanche triggering process.

[88] The present simulation does not consider erosion and dragging of granular material located beneath the initial slip surface (i.e., the surface of rupture and the surface of separation are fixed). In natural conditions, the displaced mass might drag underlying material, smoothing ''asperities'' along the slip surface and eventually modifying avalanche motion; in particular, avalanche basal erosion may smooth the convex up geometry of the slip surface at the toe of the dip slope, reducing extensional granular flow observed in the final stage of avalanche motion when the SS dips downslope (see section 4.4). This process may be analyzed by considering granular models in which the boundaries are located in the rock volume underlying the slip surface.

[89] This approach can be adapted to study the frequency and volume distribution of successive avalanches from the same slope. The characteristic time and volume scales are controlled by four interconnected factors: the degradation of strength properties of shallow rocks, the morphologic input (e.g., river incision and footslope erosion), the hydrological input (e.g., rainfall infiltration), and the tectonic input (e.g., seismic shaking and tilting). For this, appropriate time- and

depth-dependent mechanical properties must be defined for shallow materials.

[90] **Acknowledgments.** The authors have appreciated valuable discussions with N. Estrada, J. Malavieille, C. Y. Lu, and F. S. Jeng. We thank M. McSaveney for a thorough review of the manuscript and an anonymous reviewer for comments on the text. This work was partially funded by the following projects: INSU Reliefs de la Terre 2005–2006, ANR ACTS-Taiwan 2006–2010, and INSU ACI Catastrophes Naturelles 2002–2004.

References

Ambraseys, N. N. (1960), On the shear response of a two-dimensional truncated wedge subjected to an arbitrary disturbance, *Bull. Seismol. Soc. Am.*, *50*, 45–56.

Angelier, J., J. C. Lee, H. T. Chu, J. C. Hu, C. Y. Lu, Y. C. Chan, T. J. Lin, Y. Font, B. Deffontaines, and Y. B. Tsai (2001), Le séisme de Chi-Chi (1999) et sa place dans l'orogène de Taiwan, *C. R. Acad. Sci.*, *33*, 5–21.

Bardet, J. P. (1997), *Experimental Soil Mechanics*, 113 pp., Prentice-Hall, Upper Saddle River, N. J.

Boore, D. M. (2001), Effect of baseline corrections on displacements and response spectra for several recordings of the 1999 Chi-Chi, Taiwan, earthquake, *Bull. Seismol. Soc. Am.*, *91*, 1199–1211.

Buss, E., and A. Heim (1881), *Der Bergsturz von Elm*, 113 pp., Worster, Zurich, Switzerland.

Campbell, C. S., P. Cleary, and M. Hopkins (1995), Large-scale landslide simulations: Global deformation, velocities, and basal friction, *J. Geophys. Res.*, *100*, 8267–8283.

Chang, K.-J., A. Taboada, and Y.-C. Chan (2005a), Geological and morphological study of the Jiufengershan landslide triggered by the Chi-Chi Taiwan earthquake, *Geomorphology*, *71*(3–4), 293–309, doi:10.1016/j.geomorph.2005.02.004.

Chang, K.-J., A. Taboada, M.-L. Lin, and R.-F. Chen (2005b), Analysis of landsliding by earthquake shaking using a block-on-slope thermo-mechanical model: Example of Jiufengershan landslide, central Taiwan, *Eng. Geol.*, *80*(1–2), 151–163, doi:10.1016/j.enggeo.2005.04.004.

Chindao (2001), Borehole investigations in theJiufengershan landslide—1 (in Chinese), technical report, Chindao Eng. Consult. Ltd. and Natl. Taiwan Univ., Taipei.

Chindao (2002), Borehole investigations in theJiufengershan landslide—2 (in Chinese), technical report, Chindao Eng. Consult. Ltd. and Natl. Taiwan Univ., Taipei.

Chugh, A. K., and T. D. Stark (2006), Permanent seismic deformation analysis of a landslide, *Landslides*, *3*, 2–12, doi:10.1007/s10346-005-0001-4.

Collins, G. S., and H. J. Melosh (2003), Acoustic fluidization and the extraordinary mobility of sturzstroms, *J. Geophys. Res.*, *108*(B10), 2473, doi:10.1029/2003JB002465.

Covey, M. (1984), Lithofacies analysis and basin reconstruction, Plio-Pleistocene western Taiwan foredeep, *Petrol. Geol. Taiwan*, *20*, 53–83.

Crespellani, T., J. Facciorusso, C. Madiai, and G. Vannucchi (2003), Influence of uncorrected accelerogram processing techniques on Newmark's rigid block displacement evaluation, *Soil Dyn. Earthquake Eng.*, *23*, 415–424, doi:10.1016/S0267-7261(03)00065-4.

Cruden, D. M., and D. J. Varnes (1996), Landslide types and processes, in *Landslides: Investigation and Mitigation*, edited by A. K. Turner and R. L. Schuster, chap. 3, pp. 36–75, Natl. Acad. Press, WAshington, D. C.

Dadson, S. J., et al. (2004), Earthquake-triggered increase in sediment delivery from an active mountain belt, *Geology*, *32*, 733–736, doi:10.1130/G20639.1.

Del Gaudio, V., R. Trizzino, G. Calcagnile, A. Calvaruso, and P. Pierri (2000), Landsliding in seismic areas: The case of the Acquara-Vadoncello landslide (southern Italy), *Bull. Eng. Geol. Env.*, *59*, 23–37.

Havenith, H.-B., A. Strom, F. Calvetti, and D. Jongmans (2003), Seismic triggering of landslides. Part B: Simulation of dynamic failure processes, *Nat. Hazards Earth Syst. Sci.*, *3*, 663–682.

Hsü, K. J. (1975), Catastrophic debris streams (sturzstroms) generated by rockfalls, *Geol. Soc. Am. Bull.*, *86*, 129–140.

Huang, C. C., Y. H. Lee, H. P. Liu, D. K. Keefer, and R. W. Jibson (2001), Influence of surface-normal ground acceleration on the initiation of the Jih-Feng-Erh-Shan landslide during the 1999 Chi-Chi, Taiwan, earthquake, *Bull. Seismol. Soc. Am.*, *91*, 953–958, doi:10.1785/0120000719.

Huang, C. S., K. S. Hsieh, and M. M. Chen (2000), Explanatory text of the geologic map of Taiwan, 1:50,000, sheet 32, Puli, technical report, Cent. Geol. Surv., Taipei.

Huang, C. S., M. M. Chen, and M. I. Hsu (2002), A preliminary report on the Jhiufenershan landslide triggered by the 21-9–1999 Chichi earthquake in Nantou, central Taiwan, *Terr. Atmos. Ocean. Sci.*, *13*, 387–395.

Huang, Y. C. (1986), Oligocene and Miocene stratigraphy of the Kuohsing area, central Taiwan, *Acta Geol. Taiwan.*, *24*, 281–318.

Hung, J. H., and D. V. Wiltschko (1993), Structure and kinematics of arcuate thrust faults in the Miaoli-Cholan area of western Taiwan, *Petrol. Geol. Taiwan*, *28*, 59–96.

Hungr, O. (2006), Rock avalanche occurrence, process and modelling, in *Landslides From Massive Rock Slope Failure*, *Earth Environ. Sci. Ser.*, vol. 302, edited by S. G. Evans et al., pp. 243–266, Springer, Dordrecht, Netherlands.

Hungr, O., and S. G. Evans (2004), Entrainment of debris in rock avalanches: An analysis of a long run-out mechanism, *Geol. Soc. Am. Bull.*, *116*, 1240–1252, doi:10.1130/B25362.1.

Ingles, J., J. Darrozes, and J.-C. Soula (2006), Effects of the vertical component of ground shaking on earthquake-induced landslide displacements using generalized Newmark analysis, *Eng. Geol.*, *86*, 134–147, doi:10.1016/j.enggeo.2006.02.018.

Itasca (2000), *FLAC—Fast Lagrangian Analysis of Continua*, Itasca Consult. Group, Minneapolis, Minn.

Jibson, R. W. (1996), Use of landslides for paleoseismic analysis, *Eng. Geol.*, *43*, 291–323.

Kao, H., and J. Angelier (2001), Stress tensor inversion for the Chi-Chi earthquake sequence and its implications on regional collision, *Bull. Seismol. Soc. Am.*, *91*, 1028–1040, doi:10.1785/0120000739.

Kramer, S. L. (1996), *Geotechnical Earthquake Engineering*, Prentice-Hall, Upper Saddle River, N. J.

Lacombe, O., F. Mouthereau, J. Angelier, and B. Deffontaines (2001), Structural, geodetic and seismological evidence for tectonic escape in SW Taiwan, *Tectonophysics*, *333*, 323–345, doi:10.1016/S0040-1951(00)00281-X.

Lee, W. H. K., T. C. Shin, K. W. Kuo, K. C. Chen, and C. F. Wu (2001), CWB free-field strong-motion data from the 21 September Chi-Chi, Taiwan, earthquake, *Bull. Seismol. Soc. Am.*, *91*, 1370–1376, doi:10.1785/0120000744.

Liao, H. W. (2000), Landslides triggered by Chi-Chi earthquake, in Chinese, M.S. thesis, Natl. Cent. Univ., Chungli, Taiwan.

Lin, A., A. Chen, C. F. Liau, C. T. Lee, C. C. Lin, P. S. Lin, S. C. Wen, and T. Ouchi (2001), Frictional fusion due to co-seismic landsliding during the 1999 Chi-Chi (Taiwan) M_L 7.3 earthquake, *Geophys. Res. Lett.*, *28*, 4011–4014, doi:10.1029/2001GL013253.

Locat, J., H. J. Lee, P. Locat, and J. Imran (2004), Numerical analysis of the mobility of the Palos Verdes debris avalanche, California, and its implication for the generation of tsunamis, *Mar. Geol.*, *203*, 269–280, doi:10.1016/S0025-3227(03)00310-4.

Mao, S., C.-Y. Huang, and Z. Lei (2002), Late Oligocene to early Miocene dinoflagellate cysts from the Kuohsing area, central Taiwan, *Rev. Palaeobot. Palynol.*, *122*, 77–98, doi:10.1016/S0034-6667(01)00144-0.

Moon, V., and H. Blackstock (2004), A methodology for assessing landslide hazard using deterministic stability models, *Nat. Hazards*, *32*, 111–134.

Mouthereau, F., O. Lacombe, B. Deffontaines, J. Angelier, and S. Brusset (2001), Deformation history of the southwestern Taiwan foreland thrust belt: Insights from tectono-sedimentary analyses and balanced cross-sections, *Tectonophysics*, *333*, 293–318.

National Center for Research on Earthquake Engineering (1999), Investigation report of the geotechnical hazard caused by Chi-Chi earthquake, Taiwan (in Chinese), technical report, Taipei.

Newmark, N. M. (1965), Effects of earthquakes on dams and embankments, *Geotechnique*, *15*, 139–160.

Pollet, N., and J. L. Schneider (2004), Dynamic disintegration processes accompanying transport of the Holocene Flims sturzstrom (Swiss Alps), *Earth Planet. Sci. Lett.*, *221*, 433–448, doi:10.1016/S0012-821X(04)00071-8.

Radjaï, F., D. E. Wolf, M. Jean, and J. J. Moreau (1998), Bimodal character of stress transmission in granular packings, *Phys. Rev. Lett.*, *80*, 61–64.

Seed, H. B. (1979), Considerations in the earthquake-resistant design of earth and rockfill dams, *Geotechnique*, *29*, 215–263.

Shin, T. C., K. W. Kuo, W. H. K. Lee, T. L. Teng, and Y. B. Tsai (2000), A preliminary report on the 1999 Chi-Chi (Taiwan) earthquake, *Seismol. Res. Lett.*, *71*, 24–30.

Shou, K. J., and C. F. Wang (2003), Analysis of the Chiufengershan landslide triggered by the 1999 Chi-Chi earthquake in Taiwan, *Eng. Geol.*, *68*, 237–250, doi:10.1016/S0013-7952(02)00230-2.

Solonenko, V. P. (1977), Landslides and collapses in seismic zones and their prediction, *Bull. Int. Assoc. Eng. Geol.*, *15*, 4–8.

Summerfield, M. A. (1994), *Global Geomorphology*, John Wiley, New York.

Suppe, J. (1980), Imbricated structure of Western Foothills belt, southcentral Taiwan, *Petrol. Geol. Taiwan*, *17*, 1–16.

Suppe, J. (1981), Mechanics of mountain building in Taiwan, *Memo. Geol. Soc. China*, *4*, 67–89.

Suppe, J., and J. Namson (1979), Fault-bend origin of frontal folds of the western Taiwan fold-and-thrust belt, *Petrol. Geol. Taiwan*, *16*, 1–18.

Taboada, A., and N. Estrada (2009), Rock-and-soil avalanches: Theory and simulation, *J. Geophys. Res.*, *114*, F03004, doi:10.1029/2008jf001072.

Taboada, A., K.-J. Chang, and J. Malavieille (2005a), Observations and simulation of force transmission in deformed conglomerates (Jiu-Jiu Fon, Taiwan), in *Powders and Grains: 5th International Conference on Micromechanics of Granular Media, Stuttgart*, vol. 1, edited by R. García-Rojo, H. J. Herrmann, and S. McNamara, pp. 73–75, A. A. Balkema, Brookfield, Vermont.

Taboada, A., K.-J. Chang, F. Radjaï, and F. Bouchette (2005b), Rheology, force transmission, and shear instabilities in frictional granular media from biaxial numerical tests using the Contact Dynamics method, *J. Geophys. Res.*, *110*, B09202, doi:10.1029/2003JB002955.

Taboada, A., N. Estrada, and F. Radjaï (2006), Additive decomposition of shear strength in cohesive granular media from grain-scale interactions, *Phys. Rev. Lett.*, *97*(9), 098302.1–098302.4, doi:10.1103/PhysRevLett.97.098302.

Veveakis, E, I. Vardoulakis, and G. Di Toro (2007), Thermoporomechanics of creeping landslides: The 1963 Vaiont slide, northern Italy, *J. Geophys. Res.*, *112*, F03026, doi:10.1029/2006JF000702.

Wang, W. N., M. Chigira, and T. Furuya (2003a), Geological and geomorphological precursors of the Chiu-feng-erh-shan landslide triggered by the Chi-Chi earthquake in central Taiwan, *Eng. Geol.*, *69*, 1–13.

Wang, W. N., H. L. Wu, H. Nakamura, S. C. Wu, S. Ouyang, and M. F. Yu (2003b), Mass movements caused by recent tectonic activity: The 1999 Chi-Chi earthquake in central Taiwan, *Island Arc*, *12*, 325–334, doi:10.1046/j.1440-1738.2003.00400.x.

Wilson, R. C., and D. K. Keefer (1983), Dynamic analysis of a slope failure from the 6 August 1979 Coyote Lake, California, earthquake, *Bull. Seismol. Soc. Am.*, *73*, 863–877.

Wu, J. H., W. N. Wang, C. S. Chang, and C. L. Wang (2005), Effects of strength properties of discontinuities on the unstable lower slope in the Chiu-fen-erh-shan landslide, *Eng. Geol.*, *78*, 173–186, doi:10.1016/j.enggeo.2004.12.005.

Wu, L. C. (1986), Palaeoenvironmental analysis of Oligocene and Miocene series in the Kuohsing area, central Taiwan, M.S. thesis, Natl. Taiwan Univ., Taipei.

Yu, S. B., H. Y. Chen, and L. C. Kuo (1997), Velocity field of GPS stations in the Taiwan area, *Tectonophysics*, *274*, 41–59, doi:10.1016/S0040-1951(96)00297-1.

K.-J. Chang, Department of Civil Engineering, National Taipei University of Technology, 1, Section 3, Chung-Hsiao East Road, Taipei 106, Taiwan. (epidote@ntut.edu.tw)

A. Taboada, UMR 5243, Géosciences Montpellier, Université Montpellier II, INSU, CNRS, CC 60, Place East Building, F-34095 Montpellier CEDEX 5, France. (alfredo.taboada@gm.univ-montp2.fr)